Mechanical Engineering Advances 2024, 2(2), 1561.
https://doi.org/10.59400/mea1561

Article

Ocean current turbine power take-off design using fluid dynamics and towing tank experiments

Setare Sadeqi[1,2], Shahab Rouhi[1,2], Nikolaos I. Xiros[1], Erdem Aktosun[3], Lothar Birk[1], Juliette Ioup[2], Miguel Trejos[1,*]

[1] Boysie Bollinger School of Naval Architecture and Marine Engineering, University of New Orleans, Louisiana 70148, USA
[2] Department of Physics, University of New Orleans, Louisiana 70148, USA
[3] Department of Shipbuilding and Ocean Engineering, İzmir Kâtip Çelebi University, Çiğli 35620, Turkey
*** Corresponding author:** Miguel Trejos, matrejos@uno.edu

CITATION

Sadeqi S, Rouhi S, Xiros NI, et al. Ocean current turbine power take-off design using fluid dynamics and towing tank experiments. Mechanical Engineering Advances. 2024; 2(2): 1561.
https://doi.org/10.59400/mea1561

ARTICLE INFO

Received: 25 July 2024
Accepted: 30 September 2024
Available online: 13 November 2024

Abstract: This study investigates the performance and power generation capabilities of a small-scale hydrokinetic turbine by comparing numerical simulations with experimental measurements. The key difference between the two models comes from the initial numerical analysis which focused only on the permanent magnet DC motor (PMDC) motor's parameters and did not account for the gear-head reduction that leads to discrepancies in current and torque predictions, especially at lower input voltages. In practice, friction losses within the gear-head increased the required current and torque, highlighting inefficiencies in the motor gear-head system. A modified experimental setup incorporated a magnetic coupling to address leakage issues and enhance system reliability. While the magnetic coupling resulted in a slight reduction in speed, current, and torque, it improved the overall integrity of the system which is essential for marine applications. The comparison between experimental results and Blade Element Momentum (BEM) simulations showed good agreement at lower speeds, but the simulations under-predicted power at higher speeds, likely due to the model's limitations in capturing complex hydrodynamic phenomena. This shows the need for comprehensive analysis, integrating both numerical and experimental approaches to optimize turbine performance. Future research will focus on refining experimental methodologies and further improving turbine design and efficiency for hydrokinetic energy systems.

Keywords: ocean current turbine (OCT); hydrokinetic turbine performance; blade element momentum (BEM) theory; magnetic coupling optimization; dynamometer testing

1. Introduction

In the rapidly advancing field of renewable energy technologies, research into ocean current turbines (OCTs) provides as a promising approach to harness the substantial energy potential of ocean currents. Ocean currents promise a reliable and consistent source of renewable energy, in contrast to the intermittent nature of wind and solar power, making OCTs a critical area of focus in sustainable energy research [1–3]. In addition to this field is the application of Blade Element Momentum (BEM) theory, which plays a crucial role in accurately simulating turbine performance by predicting hydrokinetic forces and optimizing designs for maximum efficiency [4–6]. By using BEM, we can evaluate how OCTs respond to various flow conditions, helping to fine-tune designs for better performance [7–12].

This paper presents a comprehensive study focused on the development and evaluation of a small-scale horizontal axis OCT. It combines advanced BEM simulations with innovative experimental techniques to enhance understanding of

turbine behavior and performance. Specifically, BEM is integrated with traditional mathematical models used for propeller blade design, which facilitates more accurate calculations of the forces acting on the turbine blades. This integration allows for a deeper analysis of turbine dynamics under varying operational conditions, providing crucial insights into both turbine efficiency and load distribution [13–17]. The focus of this research is to improve the design of turbine blades by adapting advanced BEM-based simulations into a refined mathematical framework tailored to OCT blade design [18–22]. Through this combination of BEM and mathematical modeling, the study manages highly accurate predictions of hydrokinetic forces, offering a more detail view of turbine behavior in real-world marine environments [23–26].

The methodology of this study is derived from the principles of marine engineering where the combination of simulation and experimentation is critical for validating these models. This combination is essential for fine-tuning the design and ensuring the reliability of OCTs under different operational scenarios [27–30]. A key part of the experimental setup is dynamometer testing which allows precise measurements of the turbine's performance. By closely monitoring the relationship between voltage, power, and rotational speed generated by the Permanent Magnet Direct Current (PMDC) motor, we can obtain detailed performance data during testing [31–35]. This process involves using a 3D-printed turbine model equipped with sensors, enabling accurate monitoring of critical performance parameters in a controlled environment [36–39]. By coupling these dynamometer tests with advanced BEM simulations, the study provides comprehensive insights into the hydrokinetic forces acting on the turbine that shows the complex interactions between blade geometry, fluid dynamics, and turbine efficiency [40–47].

The reliability of BEM simulations is further validated through careful comparisons with other experimental and theoretical models. In this context, the study emphasizes the importance of precise measurements and a comprehensive understanding of hydrodynamic effects to improve the accuracy of BEM predictions. This approach emphasizes the necessity of integrating both simulation and experimentation to achieve a better understanding of OCT behavior under various conditions [48–54]. A significant result in the study was the successful resolution of an issue encountered during earlier OCT tests—minor leakage during prolonged operation. The problem was addressed by redesigning the nacelle and incorporating a magnetic coupling system, which completely eliminated water leakage and extended the testing duration. This innovation is crucial for improving the reliability of OCTs, particularly when operating at different rotational speeds [55]. This achievement not only advances our understanding of small-scale OCT performance but also contributes to the design of more robust and efficient turbines for future applications [56–58].

A defining characteristic of this research is its interdisciplinary approach, which combines mathematical modeling, experimental validation, and innovative engineering design. This multifaceted methodology enhances the study of hydrokinetic energy conversion by providing a deeper understanding of the challenges and opportunities in OCT development. By incorporating state-of-the-art computational techniques, such as those employed in hydrodynamic modeling [59], this research shows a robust framework for optimizing turbine performance and scaling the technology for future energy needs.

In this study, we aim to evaluate and enhance the performance of a small-scale horizontal axis OCT through a combination of numerical simulations and experimental testing. Using BEM theory, this research seeks to accurately model the hydrodynamic forces acting on the turbine and validate these findings with experimental data from a redesigned turbine setup. The study also addresses mechanical inefficiencies caused by gear-head friction and explores the potential of magnetic coupling to prevent water leakage during operation. By improving turbine efficiency, reliability, and design; this research contributes to the optimization of hydrokinetic energy conversion, making the foundation for future advancements in OCT technology.

2. Methods

Numerical method

Before introducing BEM theory for the numerical analysis of OCT performance, it is essential to first establish a foundation with the actuator disc concept which forms a crucial part of turbine analysis. The actuator disc model simplifies a turbine to an idealized, actuator disc that extracts energy from the flow. This concept was first introduced by Froude through classical momentum theory which is built on several key assumptions: the flow is inviscid, incompressible, irrotational and both velocity and pressure are uniform inflow. The actuator disc concept allows for the approximation of the forces exerted by the turbine on the fluid, simplifying the analysis of how energy is extracted from the flow. By applying momentum conservation and energy principles, this model provides insight into how the turbine influences the surrounding flow, both upstream and downstream. This theoretical foundation is instrumental in understanding how OCTs convert kinetic energy from ocean currents into usable mechanical energy. By first examining this simplified model, we can better appreciate the more complex analysis provided by BEM theory, which takes into account the detailed geometry of the blades and other factors that influence the turbine's real-world performance.

To simplify the analysis, we will begin by replacing the OCT with an actuator disc inflow to capture kinetic energy while disregarding any specific turbine design characteristics for now. As shown in **Figure 1**, the downstream section has a larger cross-sectional area than the upstream section, which is smaller than the area of the actuator disc. The flow rate of water through the channel at any given cross-section is represented by AU. Applying the principle of mass conservation, we get:

$$\rho A_\infty U_\infty = \rho A_d U_d = \rho A_w U_w \quad (1)$$

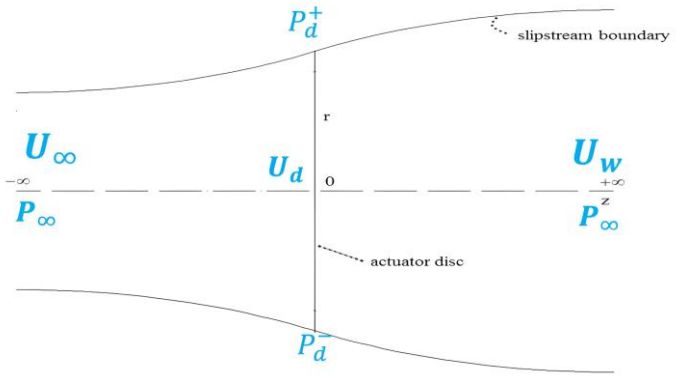

Figure 1. Actuator disc model and stream-tube concept.

The conditions of the upstream (current speed), actuator disc, and downstream are indicated by the subscripts, *d* and *w*. Due to the actuator disc's axial induction factor, *a*, which causes some variation in the current velocity,

$$U_d = U_\infty(1 - a) \tag{2}$$

We must also take the tangential flow induction factor a' into account by considering tangential velocity in addition to axial velocity. There is zero tangential velocity upstream, $2\Omega r a'$ tangential velocity is present near the actuator disc downstream, and $\Omega r a'$ tangential velocity is present in the wake.

Now let's introduce the BEM numerical analysis. BEM theory is a widely used method for predicting the performance of wind and OCTs. Blade element theory divides each rotor blade into small segments, or blade elements, treating each as a separate hydrofoil to calculate hydrodynamic forces like lift and drag based on factors such as angle of attack, pitch angle, and rotational speed. Momentum theory simplifies the overall rotor analysis by modeling the rotor as a single actuator disc that extracts kinetic energy from the flow, resulting in changes to the fluid's velocity and direction downstream, providing estimates for thrust and power generation. BEM theory integrates these approaches by calculating the forces on each blade element and using momentum theory to determine the total thrust, power, and efficiency, while also accounting for wake effects like induced velocity. Replacing the actuator disc with a 3-blade OCT, as shown in **Figure 2**, the net tangential velocity from blade element theory is $\Omega r\,(1 + a')$, defining the resulting velocity accordingly.

Axial and tangential induction factors are determined by understanding how the aerodynamic lift (C_l) and drag (C_d) coefficients vary with respect to the angle of attack for each cross-section of the blades. **Figure 3** illustrates the application of the laws of conservation of momentum and energy with a single OCT featuring with *N* blades and varying chord lengths and pitch angles, across 25 distinct cross-sections.

$$\sin\varphi = \frac{U_\infty(1 - a)}{W} \tag{3}$$

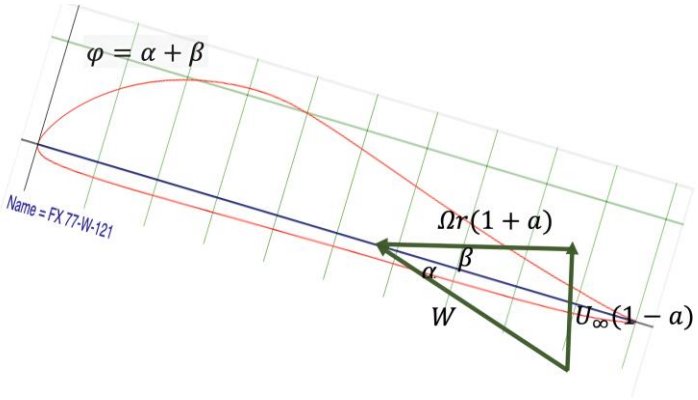

Figure 2. Velocities across the foil cross-section.

$$\cos\varphi = \frac{\Omega_r(1+a')}{W} \tag{4}$$

where $\varphi = \alpha + \beta$, based on the descriptions of the hydrodynamic forces for each cross-section. **Figure 3** shows the definitions of the cross-sectional lift and drag forces.

$$\delta L = \frac{1}{2}\rho W^2 c C_l \delta r \tag{5}$$

$$\delta D = \frac{1}{2}\rho W^2 c C_d \delta r \tag{6}$$

$$\delta L\cos\varphi + \delta D\sin\varphi = \frac{1}{2}NC\rho W^2(C_l\cos\varphi + C_d\sin\varphi)\delta r \tag{7}$$

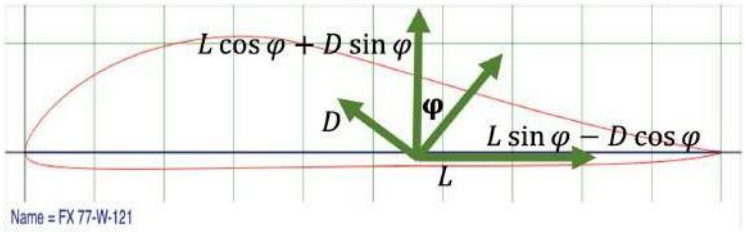

Figure 3. Lift and drag forces on the foil cross-section.

It is practical to use:

$$\mu = \frac{r}{R} \tag{8}$$

$$C_x = C_l\cos\varphi + C_d\sin\varphi \tag{9}$$

$$C_y = C_l\sin\varphi - C_d\cos\varphi \tag{10}$$

$$\frac{a}{a-1} = \frac{\sigma_r C_x}{4\sin\varphi^2} \tag{11}$$

Because the system is nonlinear, the following equations are used in an iterative process to derive the axial and tangential induction factors based on the two-dimensional hydrofoil characteristics.

$$\frac{a}{1+a'} = \frac{\sigma_r C_v}{4\sin\varphi\cos\varphi} \tag{12}$$

where σ_r is the chord solidity, calculated by dividing the circumferential length at a particular radius by the entire length of the total chord length of the blade. Note that the BEM hypothesis is valid only under the condition of uniform blade rotations.

$$\sigma_r = \frac{Nc}{2\pi r} = \frac{Nc}{2\pi\mu R} \tag{13}$$

When the effect primarily influences the blade tips by reducing the lift force and generating additional torque, it is referred to as tip loss. This phenomenon results in decreased torque that corresponds to a reduction in power. According to Ludwig Prandtl's tip loss factor, we have the following:

$$F = \frac{2}{\pi}\cos^{-1}\left(e^{-f}\right) \tag{14}$$

$$f = \frac{N(R-R)}{2r\sin\varphi} \tag{15}$$

$$\frac{r}{R} = 0.6 : F \approx 1 \& \frac{r}{R} > 0.6 : F < 1 \tag{16}$$

In addition, new equations can be derived to determine the induction factors by incorporating the tip-loss factor into the iterative solutions.

$$a = \frac{1}{\frac{4F\sin\phi^2}{\sigma_x C_x} + 1} \tag{17}$$

$$a' = \frac{1}{\frac{4F\sin\phi\cos\phi}{\sigma_y C_y} - 1} \tag{18}$$

$$\delta Q = 4\pi\rho U_\infty a'(1-a)\Omega r^3 \delta r \tag{19}$$

$$\delta P = \Omega\delta Q = 4\pi\rho U_\infty a'(1-a)\Omega^2 r^3 \delta r \tag{20}$$

Table 1 specifies the machine used to run all codes and obtain the numerical results.

Table 1. Specifications of the machine used to execute the codes and obtain the numerical results.

Component	**Specification**
Processor	12th Gen Intel(R) Core (TM) i5-12400F 2.50 GHz
RAM	32.0 GB (31.9 GB usable)
System Type	64-bit operating system, x64-based processor
Matlab Software	R2013b version

The projected shaft power and torque can be calculated using the designed rotor

at its design rotational velocity of 500 RPM with momentum theory. A detailed explanation of the BEM theory is provided in [39] and [60]. These references present a detailed background on the theoretical foundations of BEM simulations. The simulations conducted in this study were carefully aligned with the experimental configurations outlined in these sources, ensuring a high degree of accuracy and consistency between theoretical predictions and experimental results. Also, the in-house developed BEM code iteratively calculates the axial and tangential induction factors and determines the sectional forces for the small-scale OCT. This procedure is given in the algorithmic steps shown in **Figure 4**.

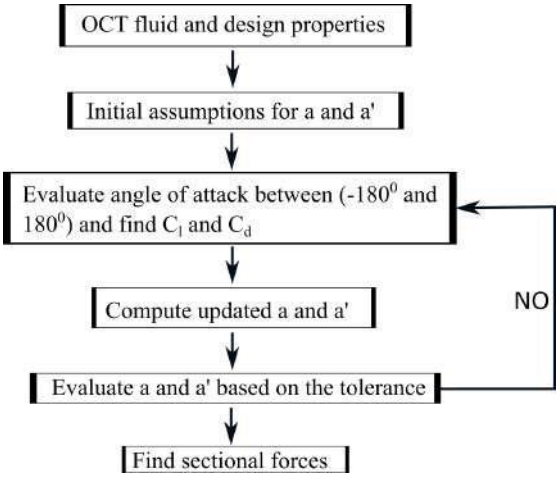

Figure 4. Algorithmic steps for BEM simulation.

3. Experimental methods

3.1. Initial experimental setup

Let's begin with the sizing of the motor/generator, sensors, and circuit components. To achieve this, the BEM theory is a well-established technique for analyzing turbine performance. In this study, an in-house BEM algorithm developed in MATLAB was employed to account for specific fluid conditions and rotor characteristics. The BEM code facilitated the estimation of various parameters, such as differential torque, thrust, and power, for the turbines under investigation. To validate the predictions obtained from the BEM code and conduct proof-of-concept testing, a small-scale, three-bladed horizontal underwater turbine was developed. Using a small-scale turbine is a cost-effective alternative to full-scale testing. This small-scale turbine served as a prototype for both testing and numerical model verification.

For the experimental setup, an electrical system was needed to meet the necessary requirements and measure the generated power. The OCT generates power based on local forces, primarily the lift force acting on the rotor blades. In addition, to prevent any structural damage to a full-scale prototype, the undesirable forces acting on the carriage were taken into account. To estimate the nominal generated power at different carriage speeds and rotor blade rotational speeds, a method was employed. The carriage speed was used to mimic the motion of the water current, which contains

kinetic energy. The tip speed ratio was adjusted to achieve optimal power production at a constant carriage speed. This adjustment was accomplished by varying the rotational speed of the rotor blades.

The design of the apparatus system was divided into two subsystems: the motor power supply and the generator power production. The motor drive power supply was responsible for converting the AC line voltage into a DC bus voltage using a switch-mode power supply. By regulating the duty cycle, the output voltage could be controlled, allowing the rotational speed of the DC motor to be varied. Prior to the design process, several considerations needed to be addressed. It was crucial to define the expectations for the entire system and determine the best approach for assembling the system with the required components. Due to the limited carriage speed in University of New Orleans towing tank facility, the DC machine needed to reach steady-state reference rotational speeds before functioning as a generator. Therefore, electricity was supplied to the motor to achieve the desired speed. Additionally, each circuit element within the system had to be carefully selected and sized to ensure proper operation.

By incorporating these considerations and implementing the described methodology, the study aimed to develop an appropriate design and gather the necessary data for further analysis and evaluation of the ocean current turbine's performance. In order to fully understand and analyze the behavior of a motor/generator, it is important to develop a comprehensive electromechanical model that precisely captures its characteristics in both motor mode and generator mode. This model serves as a fundamental requirement for studying the machine's performance and conduct. One approach to determining the characteristics of the motor/generator is through numerical analysis using computer simulation. By creating a numerical model of the machine and simulating its operation under various conditions, we can obtain valuable insights into its electromechanical behavior. Computer simulations enable us to study the machine's performance, efficiency, torque-speed characteristics, and other significant parameters. Additionally, to validate the accuracy of the numerical analysis and simulations, it is crucial to compare the simulation results with experimental data collected from the same motor/generator operating in both modes. This comparison helps in confirming the model's predictive capabilities and ensures that it accurately represents the present behavior of the machine.

By combining numerical investigations, computer simulations, and experimental data, we can develop an extensive comprehension of the machine's electromechanical characteristics. This knowledge is vital for optimizing the machine's performance, designing control strategies, and making informed decisions regarding its practical applications.

The fundamental principle of induction allows DC motors to work as generators. When a DC motor operates as a generator, the movement of a conductor in a magnetic field induces a voltage across the conductor. In this case, the induced voltage is directly proportional to the speed of the motor's shaft. The induced voltage generated by a DC motor used as a generator can be harnessed and utilized. This principle finds practical applications in the regenerative braking of electric vehicles and renewable energy systems, where energy regeneration or recovery is desired. This relationship holds true when the generator is not connected to an external load.

$$V_{ind} = \frac{\omega}{K_s} \tag{21}$$

where V_{ind} is the generated voltage (*V*), ω is the motor shaft speed (*rpm*), K_s is the speed constant of the motor, aka, speed equation constant (*rpm/V*). The speed constant is the inverse of the motor voltage constant (K_e).

$$K_s = 1/K_e \tag{22}$$

When a DC generator is loaded with current, the induced DC voltage at its terminals is reduced due to the presence of motor resistance. The motor resistance causes a voltage drop across the internal components of the generator, which reduces the voltage available at the terminals. Hence, we can rewrite Equation (21) as follows:

$$V_t = \frac{\omega}{K_s} - R_m I_l \tag{23}$$

where V_t is the generated voltage (*V*), ω is the motor shaft speed (*rpm*), K_s is the speed constant of the motor (*rpm/V*), R_m is the motor resistance (Ω), I_l is the current that goes through the wire (*A*).

To analyze the characteristics of a generator, we can plot a voltage-current curve using an equation that describes the relationship between the generated voltage and the load current. The maximum possible generated voltage is achieved when there is no load current flowing through the generator, which is also known as an open circuit condition. At this point, the generator is not connected to any external load, allowing the maximum voltage to be generated. Conversely, the maximum load current corresponds to the no-voltage induction condition, also known as a short circuit. In this situation, the generator is connected directly to a load with minimal impedance, causing the induced voltage to drop to zero. At this point, the maximum current flows through the generator. By plotting the voltage-current line, we can visualize the generator's behavior and determine its operational limits. The line can help identify the generator's voltage regulation capabilities, efficiency, and optimal operating points for different load conditions. Therefore, the maximum load current is:

$$I_{l_{max}} = \frac{\omega}{K_s} R_m \tag{24}$$

The torque required to drive the generator in order to overcome the generator internal losses and produce the load current is given by Equation (25).

$$\tau = K_t (I_l + I_o) \tag{25}$$

where τ is the required driving torque (*Nm*), I_l is the current through the wire (*A*), I_0 is the motor no-load current (*A*) corresponding to the internal torque losses, K_t is the motor torque constant or motor constant (*Nm/A*). The torque constant is equal to the motor voltage constant (K_e).

$$K_t = K_e \tag{26}$$

The generator power consists of two components, electrical output power and mechanical input power.

The electrical output power can be calculated using Equation (27).

$$P_e = V_t I_l \tag{27}$$

where P_e is the electrical power (W), V_t is the generated voltage (V), I_l is the load current (A). The maximum electrical output power at a given speed can be found from Equation (28).

$$P_{e_{Max}} = \frac{\pi}{30000} \frac{\omega^2}{4} \frac{\Delta\tau}{\Delta\omega} \tag{28}$$

where P_eMax is the maximum electrical output power (W), ω is the motor shaft speed (rpm), ($\frac{\Delta\tau}{}$) is the motor speed-torque gradient (rpm/Nm). Similarly, the mechanical input power can be calculated using Equation (29).

$$P_m = \frac{\pi}{30} \omega\tau \tag{29}$$

where P_m is the mechanical power (W), ω is the motor shaft speed (rpm), and τ is the driving torque (Nm). In general, efficiency is described as the ratio of useful output to total input. Hence, the generator efficiency is measured as the ratio of electrical output power to mechanical input power.

$$\eta_g = \frac{P_e}{P_m} \tag{30}$$

where η_g is the generator efficiency, P_e is the electrical power (W), and P_m is the mechanical power (W).

When a machine operates as a generator, its efficiency corresponds to that of its motor efficiency. Typically, a generator tends to achieve higher efficiency at higher rotational speeds. This implies that when the machine works at a faster rotational speed, it is more proficient in converting mechanical power into electrical power. Higher speeds often result in reduced losses and improved efficiency. Nonetheless, it's critical to note that the maximum efficiency of the generator occurs at a lower load current, while maintaining a given rotational speed. In other words, the generator operates most efficiently when the load associated to it draws a lower current. At lower load currents, the losses within the generator are minimized, allowing for a higher overall efficiency. Designing systems that operate the generator at higher rotational speeds while considering the appropriate load conditions can assist maximize overall efficiency and energy conversion.

In a PMDC motor, the speed of the motor can be constrained by adjusting the input voltage provided to the motor. By varying the motor voltage, we can control its rotational speed. The relationship between the angular speed (rotational speed) of the PMDC motor and the input voltage can be determined by examining the equivalent circuit of the motor. The equivalent circuit provides a simplified representation of the motor's electrical characteristics. The equivalent circuit of a PMDC motor typically consists of a voltage source, an internal resistance, and an inductor. The system equation of a PMDC motor is given by applying Kirchhoff's voltage law:

$$E_a = R_a i_a(t) + L_a\, ia(t) + E_b \tag{31}$$

where E_a is the applied voltage (V), R_a is the terminal resistance (Ω), i_a is the armature current (A), L_a is the terminal inductance (H), and E_b is the back electromotive force

(*V*). Further system equations are:

$$E_b = K_e\omega(t) \tag{32}$$

where K_e is the back-emf constant (*V/rad/s*), and ω is the angular speed (*rad/s*).

$$T = K_T i_a(t) = b\omega(t) + J\frac{d\omega(t)}{dt} \tag{33}$$

where *T* is the generated torque (*Nm*), K_T is the torque constant (*Nm/A*), *b* is the motor friction coefficient (e.g., brushes) (Nm s), and *J* is the load and armature inertia (kg m^2).

$$\frac{d\theta(t)}{dt} = \omega(t) \tag{34}$$

where θ is the rotor angular position (rad). In the case of a constant operating point, this equation can be simplified as follows:

$$E_a = R_a i_a + E_b \tag{35}$$

Thus, the electrical input power can be calculated by multiplying voltage by current:

$$E_a i_a = R_a i^2 + K_e\omega i_a \tag{36}$$

Mechanical output power is equal to torque times rotational speed:

$$T\omega = K_T\, i_a\omega \tag{37}$$

Electrical losses are caused by the resistance in the circuit:

$$Losses = R_a i_a^2 \tag{38}$$

To develop a model based on these equations, the values of the motor parameters must be defined. Simulations were performed for the PMDC motor using the motor parameters shown in **Table 2**. The models were implemented in a MATLAB environment.

The primary objective of this investigation is to determine the characteristic parameters of a PMDC motor operating in both motor and generator modes. This PMDC motor was selected to be used as a small-scale experimental hydrokinetic turbine. To achieve this objective, an experimental setup was designed. The PMDC motor, chosen as the prime mover, was mechanically connected shaft to shaft to an identical PMDC motor configured as a generator. This mechanical connection allowed for the transfer of mechanical power between the two motors.

Table 2. Key data of PMDC motor.

Motor Data	**Units**	**Values**
Nominal Voltage	V	12
No Load Speed	rpm	8130
No Load Current	A	0.32
Speed Constant	rpm/V	699
Torque Constant	Nm/A	0.0137

Table 2. (*Continued*).

Motor Data	Units	Values
Motor Resistance	Ω	0.079
Rotor Inertia	gcm2	99.5
Braking Load Resistance	Ω	1
Load Torque	Nm	0.12

In the experiment, a time-varying input voltage was applied to the prime mover motor, which effectively altered its rotational speed. The speed of the prime mover motor, in turn, forced the generator motor to generate a voltage. This voltage generated by the generator motor varied in amplitude corresponding to the input voltage applied to the prime mover motor.

On the generator side of the circuit, a variable resistor, denoted as "*R*", was manually adjusted. This variable resistor acted as a changeable load within the system. By altering the value of this resistor, the load on the generator motor could be modified, impacting the electrical characteristics of the system.

By manipulating the input voltage applied to the prime mover motor and adjusting the variable resistor on the generator side, the experiment allowed for the collection of data on the generator's performance under different load conditions. This data would enable the determination of important characteristic parameters of the PMDC motor, such as voltage-current relationships, power output, efficiency, and other relevant performance metrics. The equivalent circuit of this setup is illustrated in **Figure 5**.

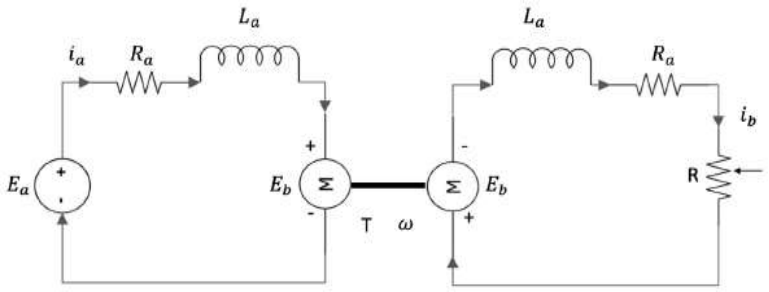

Figure 5. Equivalent circuit of the experimental setup.

The system behavior of the dynamometer is given by applying Kirchhoff's voltage law on both circuits knowing that the armature resistor, armature inductance, angular speed, and the amount of the torque are the same.

Power circuit:

$$E_a = R_a i_a(t) + L_a \frac{di_a(t)}{dt} + K_e \omega(t) \tag{39}$$

Load circuit:

$$E_b = R_a i_b(t) + L_b \frac{di_b(t)}{dt} + K_e i_b(t) \tag{40}$$

where R is the variable resistor (Ω) and i_b is the generated current (A). In the case of a constant operating point, these above equations can be simplified as follows:

Power circuit:

$$E_a = R_a i_a + K_e \omega \tag{41}$$

Load circuit:

$$K_e \omega = (R_a + R) i_b \tag{42}$$

To evaluate the performance and efficiency of the PMDC motor operating in both motor mode and generator mode, certain parameters need to be measured. These parameters include the input voltage, motor parameters, and the shaft angular speed. By utilizing these equations, it becomes possible to estimate the current flowing in both the power circuit and the load circuit. Once the currents in both circuits are estimated using the equations, it becomes possible to calculate the input power and the generated power. By considering the currents and voltages, along with the input power and generated power, it becomes feasible to assess and analyze the performance and efficiency of the PMDC motor. These calculations give valuable insights into how effectively the motor converts electrical power into mechanical power when operating in motor mode and how efficiently it converts mechanical power into electrical power while working as a generator.

To enhance the accuracy of the estimations regarding generated power and input power from numerical analysis, a specific experimental setup was employed including two identical PMDC motors.

- Connection of PMDC Motors: The two PMDC motors were mechanically connected shaft to shaft. This setup allowed us to not just assess the performance of the PMDC motor as a prime mover (when it drives the turbine) yet additionally as a generator (when it produces electrical power).
- Variable DC Voltage Source: A variable DC voltage source was connected to one of the PMDC motors, known as the prime mover motor (type DCX 35 L with a power rating of 80/120 Watts). By changing the input voltage provided to this motor, its rotational speed is adjusted.
- Gearhead for Speed Adjustment: The PMDC motor has a characteristic speed rate of 8130 RPM. However, due to the fact that the turbine was scaled down in size for experimentation, a planetary gearhead (type GPX 37) with a reduction ratio of 16:1 was utilized. This gearhead reduced the motor's speed to a more suitable level for the scaled-down turbine
- Rotary Torque Sensor: A TRS605 non-contact shaft-to-shaft rotary torque sensor with an encoder was placed between the prime mover and generator shafts. This allowed us to measure the driving torque applied and the rotational speed of the system.
- Servo Motor Driver: To control the speed of the prime mover PMDC motor, an ESCON 50/5 servo controller was utilized as a regulator. This controller allowed us to fix a setpoint value for the motor's speed, providing precise command over the motor's rotational speed during testing.

The experimental setup, as described above, is visually depicted in **Figure 6**.

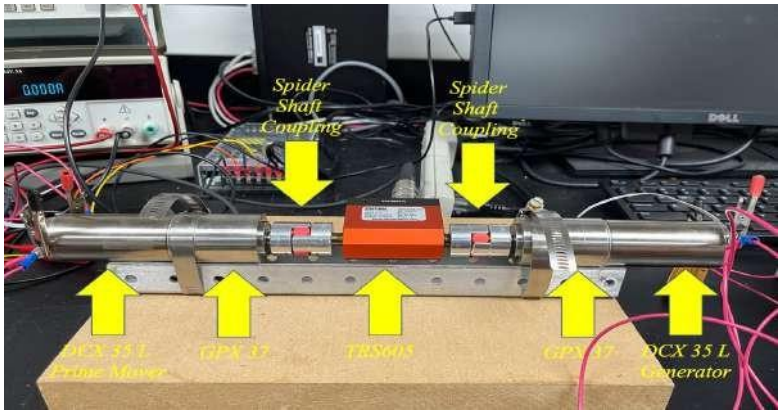

Figure 6. Initial experimental setup.

This setup was carefully intended to provide accurate and reliable data for assessing the performance of the hydrokinetic turbine PMDC motor under various conditions. By measuring torque, speed, and controlling the motor's speed with precision, we can obtain valuable insights into the turbine's PMDC motor behavior and efficiency during experimentation. The data acquisition system incorporates sensors that monitor the electrical current and voltage on both sides of the system, namely the power circuit (supplying electrical power to the prime mover PMDC motor) and the load circuit (where the generated power is utilized). These sensors allow us to measure and analyze the electrical characteristics of the turbine during testing.

To alter the speed of the prime mover, the input voltage is manually adjusted to the motor driver. The generator, mechanically connected to the prime mover, was forced to produce a voltage as a result of this connection. Varied load resistor utilized to assess the system's performance under different conditions. However, there is a restriction on the size of the load resistor. At the point when a smaller load resistor is used, the current flowing through the system increased, resulting in higher power output. This relationship between load resistor size, current, and power is a significant consideration for testing the turbine's efficiency and power generation capabilities. The PMDC motor used in the experiment had the power rating modes: 80 Watts in continuous operation mode and 120 Watts in intermittent operation mode. The decision of the specific motor and its power rating modes were likely based on the requirements and characteristics of the hydrokinetic turbine model.

The reason for using a PMDC motor with a planetary gearhead combination was because of the slow-moving nature of the driving mechanism in ocean current turbines. The turbine model expected a slower rotational speed to match the characteristics of ocean currents. However, this gearing combination presented difficulties when using the motor as a generator. Reversing the motor to function as a generator caused inefficiencies because the two-stage gearhead is not originally intended for such utilization. As a result, the generator mode may not achieve the same level of efficiency as the prime mover mode, impacting the overall performance and power generation capability of the hydrokinetic turbine.

Figure 7 compares two models: one derived from numerical analysis and the other based on actual experimental measurements. The difference between the two models can be attributed to a key factor: the calculations in the numerical analysis

were initially based solely on the PMDC motor's parameters, without accounting for the effect of the gearhead reduction. In other words, the numerical analysis focused on the PMDC motor itself, neglecting the influence of the attached gearhead.

In practical experiments, however, the gearhead's reduction effect becomes significant and needs to be accounted for. The figure illustrates that at lower voltage levels, the measured current from experiments is higher than what was initially predicted by the numerical analysis. The reason for this discrepancy is that, at lower voltages, more current is required to compensate for the losses caused by friction within the gearhead. Friction within the gear-head can result in energy losses, making the actual motor-gearhead system less efficient than predicted by the numerical analysis. As a consequence, a higher current is needed to achieve the expected performance level during the experimental measurements.

This observation highlights the importance of considering all components and their interactions in the system when conducting numerical analysis or simulations.

Figure 8 presents a correlation between the rotational speed of the PMDC motor, which was operated as a prime mover, under different input voltage conditions. In the figure, the black solid line represents the rotational speed calculated from numerical analysis, while the square points represent the measured rotational speed obtained from actual experimental testing. The comparison in **Figure 7** reveals that the measured angular speed of the experimental PMDC motor is lower compared to the angular speed predicted by the numerical analysis. The reason for this inconsistency is attributed to the presence of the planetary reduction gearhead.

Figure 9 gives a comparison of the torque delivered by the PMDC motor at different input voltages, alongside the measured torque obtained during experimental testing. In the figure, the black line represents the torque values determined from numerical analysis, while the red line represents the torque values measured during the actual experiment. The comparison in **Figure 6** reveals that the measured torque (squre points) during the experimental testing is different from the torque values estimated by the numerical analysis (black solid line). The reason for this difference is attributed to the presence of the gearhead attached to the PMDC motor. When operating at lower input voltages, the measured torque is higher than the torque values estimated by the numerical analysis. This is because at lower voltages, the motor requires more current to compensate for the friction losses within the gearhead. As mentioned previously, the gearhead introduces mechanical inefficiencies and losses. These losses impact the actual torque output of the motor during experiments, resulting in a higher measured torque compared to what was initially anticipated in the numerical analysis.

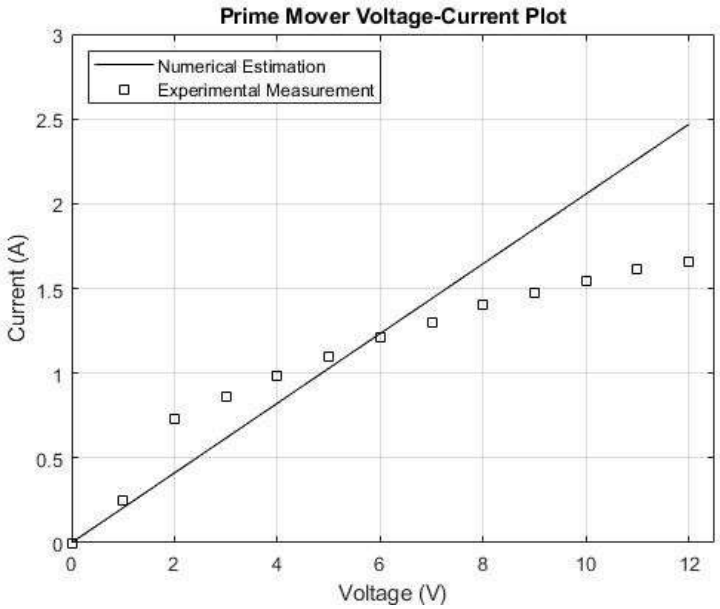

Figure 7. Current comparison at different input voltages between numerical and experimental models.

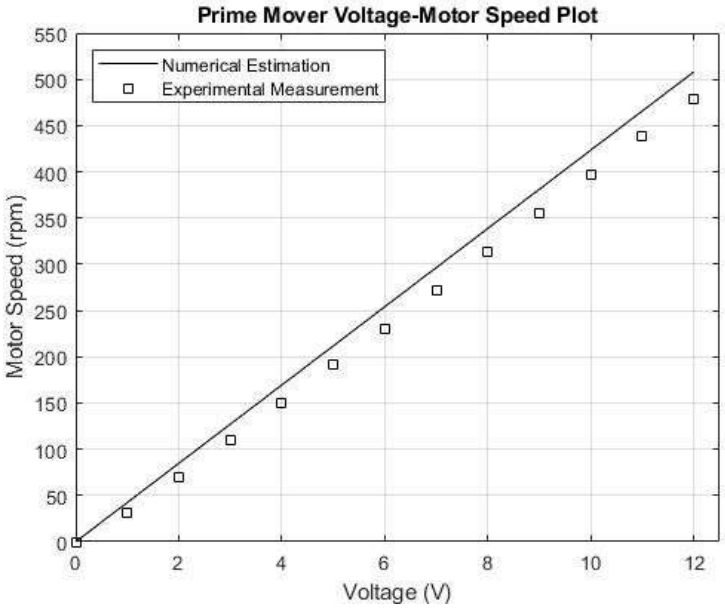

Figure 8. Rotational speed of the PMDC motor under varying input voltages.

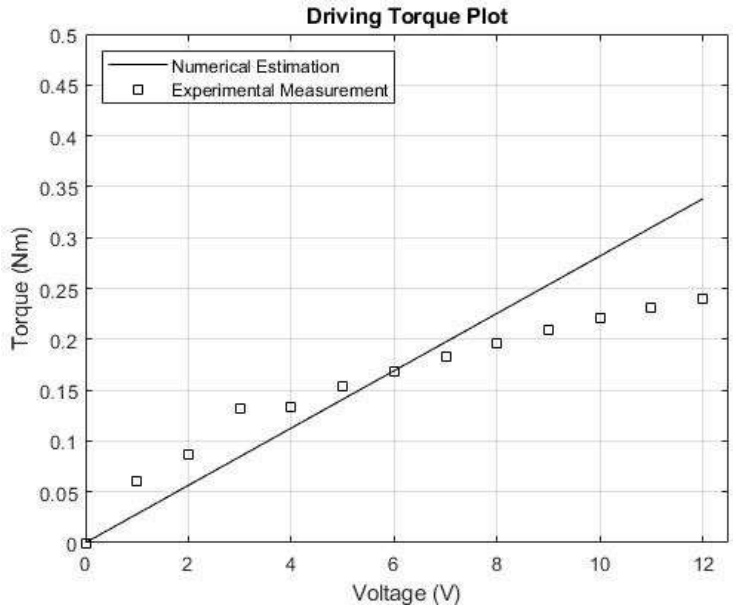

Figure 9. Torque comparison at different input voltages between numerical estimation and experimental measurements.

In summary, as it is represented the influence of the gearhead on the performance of the PMDC motor. The presence of the gearhead leads to discrepancies between the estimated values from numerical analysis and the measurements during experimental testing, especially at lower input voltages. Understanding the impact of the gearhead on PMDC motor output is important for accurately assessing the performance of the hydrokinetic turbine model and optimizing its design and efficiency.

3.2. Modified experimental setup

In this section, we revise the dynamometer characterization testing with a focus on magnetic coupling as shown in **Figure 10**. The primary objective of this revised testing is to determine the characteristic parameters of a PMDC motor configured for use as a small-scale experimental hydrokinetic turbine. Unlike the initial design, the dynamometer now features a redesigned magnetic coupling to address previous issues related to leakage. The fundamental principle remains unchanged, with the PMDC motor serving as a prime mover connected shaft-to-shaft to an identical PMDC motor configured as a generator.

The dynamometer's behavior is governed by Kirchhoff's voltage law, considering identical armature resistors, armature inductances, angular speeds, and torques in both the power and load circuits. The power circuit equation is given by:

Power circuit:

$$E_a = R_a i_a(t) + L_a \frac{di_a(t)}{dt} + K_e \omega(t) \tag{43}$$

Load circuit:

$$E_b = R_a i_b(t) + L_b \frac{di_b(t)}{dt} + K_e i_b(t) \tag{44}$$

where R is the variable resistor (**Ω**) and i_b is the generated current (A). In the case of a

constant operating point, these equations can be simplified as follows:

Power circuit:

$$E_a = R_a i_a + K_e \omega \tag{45}$$

Load circuit:

$$K_e \omega = (R_a + R) i_b \tag{46}$$

To enhance accuracy, a specific experimental setup is employed, incorporating two identical PMDC motors. The connection of PMDC motors, a variable DC voltage source, gearhead for speed adjustment, rotary torque sensor, and a servo motor driver is maintained from the initial design. The key modification is the introduction of a redesigned magnetic coupling to address leakage issues and enhance system reliability.

This setup ensures precise control over the prime mover's speed and allows for comprehensive data collection on torque, speed, and electrical characteristics.

Let's talk about impact of magnetic coupling. The introduction of the magnetic coupling into the system has a subtle impact on the overall performance. One notable effect is a slight reduction in the rotational speed when compared to both the initial dry test and the numerical results as shown in **Figure 11**.

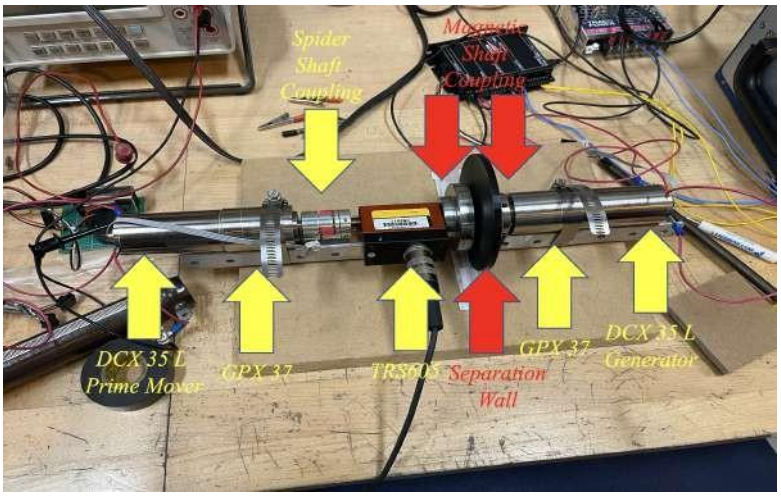

Figure 10. Revised experimental setup.

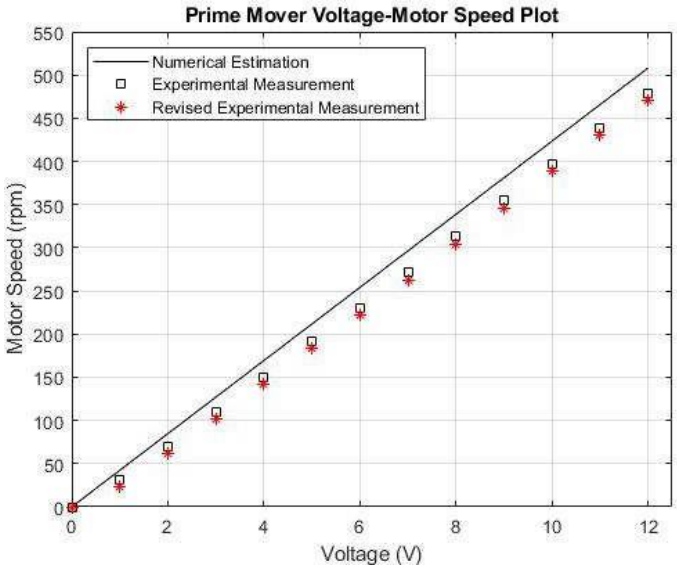

Figure 11. Detailed comparative analysis of revised prime mover voltage-motor speed.

The incorporation of the magnetic coupling into the system has led to a marginal decrease in both the generated current (**Figure 12**) and generated torque (**Figure 13**) in comparison to the initial dry test. This outcome aligns with expectations, considering the observed reduction in rotational speed.

The introduction of a magnetic coupling in the system, while resulting in a minor reduction in overall performance, is deemed essential due to its pivotal role in preventing shaft leakage—a critical issue faced in the initial design. The compromise in performance, evidenced by a slight decrease in rotational speed, generated current, and torque, serves as a trade-off for the enhanced system integrity achieved through the magnetic coupling's ability to seal the shaft. In marine applications, where exposure to corrosive elements is a significant concern, the magnetic coupling proves invaluable by providing a hermetic seal without the need for traditional seals susceptible to wear and corrosion. The technology's benefits include reduced maintenance, enhanced reliability, and resistance to corrosion, positioning magnetic couplings as crucial components in marine systems, aligning with the imperative for robust and durable solutions in challenging environments.

We addressed the nacelle redesign and reconstruction following the initial experiment, as detailed in [37]. During this experiment, a leakage issue was identified around the propeller pipe, indicating that water was escaping from the area surrounding the propeller. This leakage posed a risk to the experiment's integrity and the turbine's functionality for further research. To resolve this issue, a magnetic coupling was implemented through the shaft. A magnetic coupling is a mechanism that transfers torque between two rotating shafts without direct physical contact, making it ideal for applications requiring a water-tight seal. It effectively prevents fluid leakage such that it enhances the system's reliability.

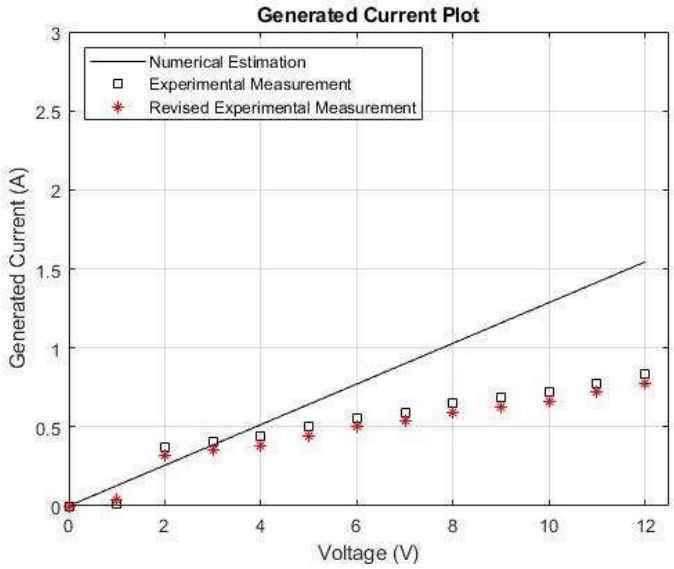

Figure 12. Detailed comparative analysis of revised generated current measurements.

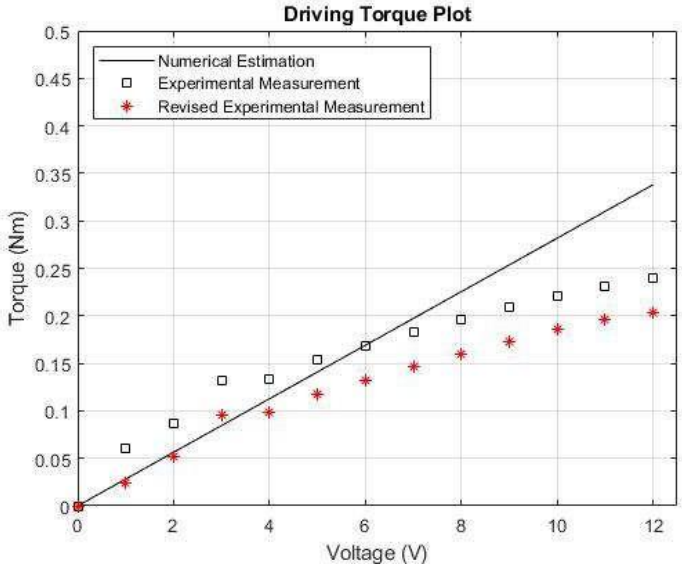

Figure 13. Detailed comparative analysis of revised torque measurements.

The next step involved redesigning the nacelle, specifically the torpedo component, to accommodate this solution and ensure water-tightness. This redesign included dividing the torpedo nacelle into two distinct segments:

- Wet Department: This segment houses the components that are exposed to water, including the propeller and the magnetic coupling mechanism.
- Dry Department: This segment is designed to remain dry and houses components that should not be exposed to water, such as electrical components or sensors.
- Wall Installation: A key feature of this redesign is the installation of a wall between the wet and dry departments of the torpedo nacelle. The magnetic coupling is placed within this wall, between the wet and dry departments. This positioning allows the magnetic coupling to function effectively while preventing any water from entering the dry department.

  The wall acts as a barrier, effectively sealing off the wet department from the dry

department. **Figure 14 (a)** shows the sketch of the wet part of the torpedo and **Figure 14 (b)** shows the sketch of front wall barrier of the nacelle. It ensures that any leakage from the propeller pipe is contained within the wet department and does not affect the dry components. The redesign was specifically implemented in the front piece of the torpedo nacelle. This piece was split into two parts, and the wall was inserted between them to create the separation between the wet and dry departments.

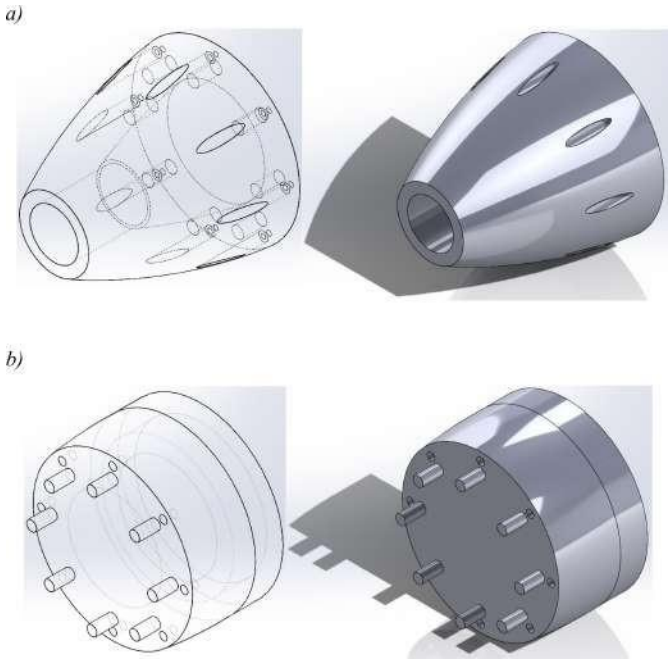

Figure 14. (a) Solidworks sketch of the wet part of the torpedo and; **(b)** solidworks sketch of the wall barrier of the front piece of nacelle.

The modification involved the use of a magnetic coupling and the redesign of the torpedo nacelle to prevent water leakage from the propeller pipe. The installation of a wall between the wet and dry departments, particularly in the front piece of the torpedo, ensures that the magnetic coupling can function as intended while maintaining a water-tight seal, enhancing the overall integrity of the experiment and data collection process. In continuity with our prior work, we implemented identical steps to augment water-tightness and mitigate the risk of leakage in the redesigned model. Employing the same procedural framework as in the previous test, the entire model underwent a thorough coating with epoxy, a robust adhesive and sealant known for its exceptional waterproofing properties as shown in **Figure 15**. This epoxy application, constituting an additional protective layer, substantially reinforces the system against water ingress. The approach mirrors the effective strategy employed during the initial test. The application of epoxy continues to serve as a resilient shield, contributing to the model's durability and reliability.

Figure 15. Revised design of nacelle coated with epoxy and its parts.

4. Results and discussion

For this round of testing, we continued using the same instrumentation as in our previous trials with a key modification in the coupling mechanism. The hydrokinetic turbine model integrates an electric motor capable of functioning as a generator, accompanied by an array of sensors, all housed within the insert. Specifically, we employed a PMDC motor of the DCX 35 L type, boasting a power rating ranging from 80 to 120 Watts, as the motor/generator.

To exert precise control over its operation, the PMDC motor was linked to a driver, facilitating regulation of the motor's speed. A variable DC voltage source, connected to the driver, was employed to adjust the motor speed by varying the input voltage. The motor, with a speed rating of 8130 RPM, was paired with a planetary gearhead (GPX 37) featuring a reduction ratio of 16:1 to accommodate the scaled-down size of the turbine model. This gearhead choice was imperative due to the model's constraint on rotational speed.

In the experimental setup, consistent with our prior work, a range of sensors and equipment was integrated to measure and control various parameters of the hydrokinetic turbine system. Notable instruments included the TRS605 Rotational Force Sensor, serving to precisely gauge driving torque and turbine rotational speed. The ESCON 50/5 Servo Controller, a motor driver, maintained a setpoint rotational speed and adjusted it as required during testing. Current sensors (ACS712) and voltage sensors (DC0-25V) were employed to measure electrical power generation, crucial for computing the generated power. Additionally, temperature and humidity sensors, consisting of SHT30 and DHT22 types, were strategically placed for safety and performance monitoring within the turbine nacelle.

Despite maintaining the consistency of the overall instrumentation from our previous testing, the magnetic coupling replaced the Spyder coupling in the current setup. The integrated sensors and equipment are visually represented in **Figure 16**.

The evaluation of hydrodynamic characteristics for the hydrokinetic turbine involved a systematic process closely mirroring our prior testing methodology. Before initiating experiments, precise positioning of the turbine model within the towing tank ensured optimal alignment and a watertight seal. Subsequently, the turbine underwent

towing at a predetermined speed, capturing vital data through installed sensors measuring torque and speed. This approach provided valuable insights into the turbine's performance under varying flow conditions.

Notably, the methodology employed in this testing phase, featuring a magnetic coupling, replicated the exact procedure utilized in previous tests. Emphasizing continuity, we maintained identical numerical values to ensure a meticulous repetition of our prior experiments. **Figure 17** visually illustrates the prototype turbine submerged in the towing tank, showcasing the consistent application of our established testing protocol.

In our nacelle redesign experiments using magnetic coupling, we apply the same protocol as in previous tests. **Figure 18 (a)** compares torque results and **Figure 18 (b)** compares power results by plotting data from three different methods: The solid line represents the numerical method using BEM theory, the black squares denote results from prior testing without magnetic coupling, and the red stars indicate measurements with magnetic coupling. The data reveal a consistent trend where, as carriage speed increases, the generated power also rises, aligning with the expectation that higher fluid speed delivers more energy to the turbine blades. Up to a carriage speed of 1.8 m/s, BEM simulations predicted slightly lower power generation compared to experiments, suggesting a possible underestimation of OCT performance by the simulations. However, beyond 2 m/s, BEM-calculated power exceeded experimental results. Discrepancies between experimental data and BEM simulations can come from several factors. One major issue may be measurement inaccuracies related to the experimental setup or the equipment used, which might not have been sufficiently precise. For instance, errors in sensor calibration or limitations in measurement resolution could contribute to these discrepancies. Also, BEM simulations might not fully capture the complex hydrodynamic effects observed in real OCTs, such as turbulence and three-dimensional flow effects, which are challenging to model accurately. These complex dynamics, particularly at varying flow speeds, might be inadequately represented by the BEM method. To sum up, the simulations may not fully reflect the actual hydrodynamic environment, leading to differences between simulated and experimental results as discussed in [60]. As noted in [60], future work might explore alternative turbine designs, materials, and sensor technologies to enhance hydrokinetic energy systems. Furthermore, measurements with the magnetic coupling exhibited slightly lower values compared to prior experimental measurements that can be attributed to the impact of the coupling on the system.

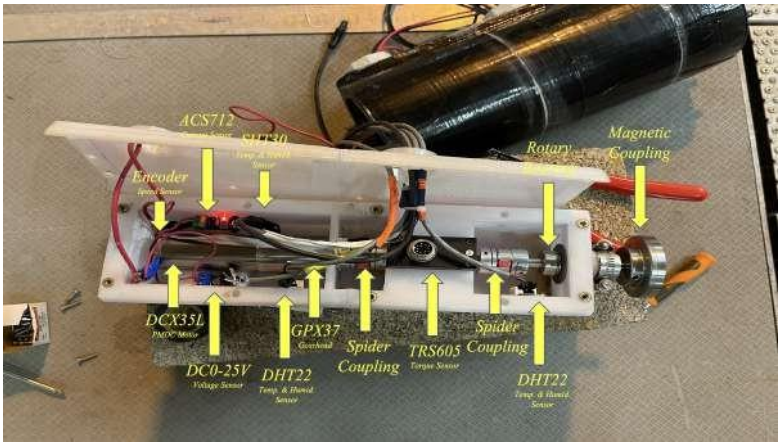

Figure 16. Electric instruments setup.

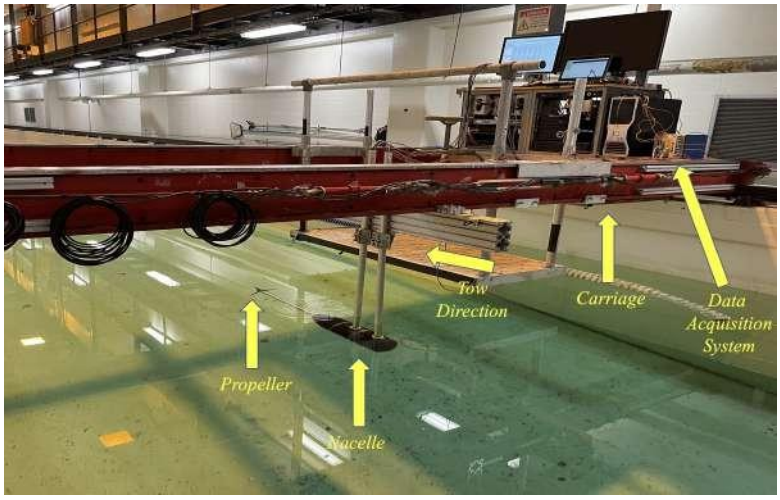

Figure 17. Photograph of the prototype turbine during the towing tank experiment.

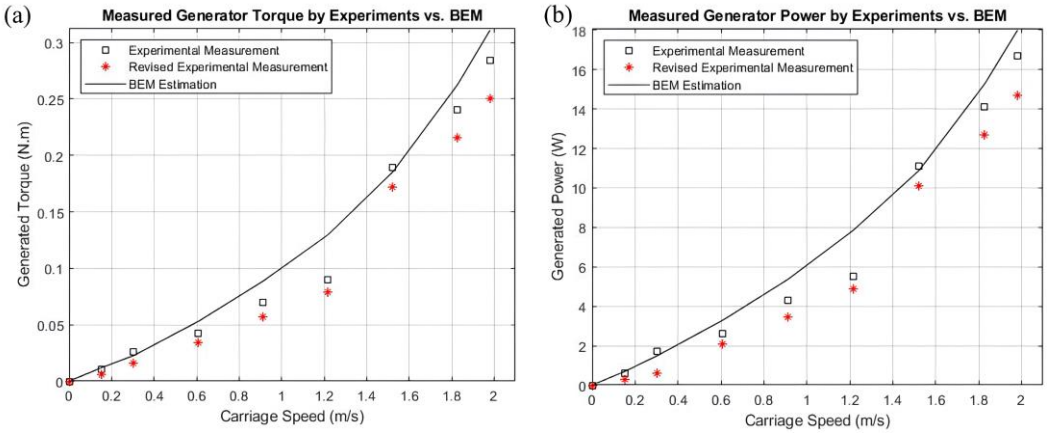

Figure 18. (a) Comparison of generated torque results and; **(b)** comparison of generated power results.

The proposed numerical method based on BEM theory shows the robustness through a strong match with experimental results and adaptability to real-world challenges as shown in [36]. Despite some discrepancies, primarily due to unmodeled hydrodynamic effects and measurement inaccuracies, the method accurately predicts power generation and hydrodynamic forces. It accounts for practical issues, such as the impact of a gear-head on motor speed and torque, and successfully incorporates

magnetic couplings to address leakage issues, enhancing system reliability. The method's comprehensive approach that combines advanced simulations with detailed experimental testing, highlights its flexibility and precision. Furthermore, the study identifies areas for future optimization, such as refining simulations to better capture complex flow dynamics, ensuring the model remains robust and capable of continuous improvement in hydrokinetic turbine design.

The study could further explore how its results influence the design and deployment of full-scale OCTs in real-world marine environments. By addressing challenges like hydrodynamic inefficiencies and leakage, the study's insights into torque, speed, and magnetic couplings can optimize larger systems. The use of magnetic couplings enhances OCT durability and reliability in corrosive marine settings. Future research could focus on scaling up turbine designs and refining simulations to improve efficiency in different ocean conditions, advancing sustainable marine energy solutions. Also, we will include additional validation of the results such as comparisons with other established models or larger-scale testing.

5. Conclusions

This study represents a significant advancement in the development and evaluation of a small-scale horizontal OCT through the use of BEM simulations. By integrating a sophisticated mathematical model with practical experimental testing, we achieved precise calculations of hydrokinetic forces and gained a deeper understanding of small-scale turbine performance. The innovative approach of combining detailed simulations with marine-inspired dynamometer testing and a 3D-printed turbine model equipped with sensors enabled comprehensive monitoring of power, force, and rotational speed during towing tank tests. The good agreement between experimental results and BEM simulations highlights the robustness of the model, although some discrepancies were observed due to factors such as measurement accuracy and hydrodynamic effects. The successful redesign, which addressed previous leakage issues by incorporating magnetic coupling, has improved the reliability and longevity of testing, providing valuable insights into turbine performance across different speeds. In the future, we plan to refine our experimental methods, especially with the new nacelle design, and conduct broader studies to further optimize efficiency, applicability, and repeatability. This interdisciplinary research, combining advanced modeling, experimental techniques, and innovative design solutions, fosters future developments in hydrokinetic energy conversion. Also, this study could further explore how its results influence the design and deployment of full-scale OCTs in real-world marine environments. By addressing challenges like hydrodynamic inefficiencies and leakage, the study's insights into torque, speed, and magnetic couplings can optimize larger systems. The use of magnetic couplings enhances OCT durability and reliability in corrosive marine settings. Future research could focus on scaling up turbine designs and refining simulations to improve efficiency in different ocean conditions, advancing sustainable marine energy solutions.

Author contributions: Conceptualization, NIX and EA; methodology, SS, SR, NIX and EA; software, EA; validation, NIX, EA and SS; formal analysis, JI; investigation, SS and SR; resources, NIX and LB; data curation, SS and SR; writing—original draft preparation, NIX, SS and EA; writing—review and editing, NIX, EA and MT; visualization, SS, EA and MT; supervision, NIX, LB and EA; project administration, NIX and LB; funding acquisition, NIX and LB. All authors have read and agreed to the published version of the manuscript.

Funding: This research was funded by the National Science Foundation (NSF) and specifically the Energy, Power, Control and Networks (EPCN) program within the framework of grant ECCS-1809182.

Acknowledgments: The authors would like to thank the National Science Foundation (NSF) and specifically the Energy, Power, Control and Networks (EPCN) program for their valuable ongoing support in this research within the framework of grant ECCS-1809182 'Collaborative Research: Design and Control of Networked Offshore Hydrokinetic Power-Plants with Energy Storage'. We express our deepest thanks to George R. Morrissey and Ryan D. Thiel for their outstanding contributions and the positive impact they have had on our research endeavors. Their invaluable guidance, technical assistance, and collaborative spirit have been integral to the success of our project.

Conflict of interest: The authors declare no conflict of interest.

References

1. Boehlert, G. W. and Gill, A. B. (2010). Environmental and ecological effects of ocean renewable energy development: a current synthesis. Oceanography, 23(2):68–81.
2. Majdi Nasab, N., Kilby, J., and Bakhtiaryfard, L. (2020). The potential for integration of wind and tidal power in new zealand. Sustainability, 12(5):1807.
3. Stevens, C., Smith, M., Grant, B., Stewart, C., and Divett, T. (2012). Tidal energy resource complexity in a large strait: The karori rip, cook straight. Continental Shelf Research, 33:100–109.
4. Lewis, M., Neill, S., Robins, P., and Hashemi, M. (2015). Resource assessment for future generations of tidal-Stream Energy arrays. Energy, 83:403–415.
5. Fox, C. J., Benjamins, S., Masden, E. A., and Miller, R. (2018). Challenges and opportunities in monitoring the impacts of tidal-Stream Energy devices on marine vertebrates. Renewable and Sustainable Energy Reviews, 81:1926–1938.
6. Brooks, D. A. (2006). The tidal-Stream Energy resource in passamaquoddy–cobscook bays: A fresh look at an old story. Renewable Energy, 31(14):2284–2295.
7. El-Shahat, S. A., Li, G., Lai, F., and Fu, L. (2020). Investigation of parameters affecting horizontal axis tidal current turbines modeling by blade element momentum theory. Ocean Engineering, 202:107176.
8. Rahimian, M., Walker, J., and Penesis, I. (2018). Performance of a horizontal axis marine current turbine–a comprehensive evaluation using experimental, numerical, and theoretical approaches. Energy, 148:965–976.
9. Dehouck, V., Lateb, M., Sacheau, J., and Fellouah, H. (2018). Application of the blade element momentum theory to design horizontal axis wind turbine blades. Journal of Solar Energy Engineering, 140(1):014501.
10. Bahaj, A., Batten, W., and McCann, G. (2007a). Experimental verifications of numerical predictions for the hydrodynamic performance of horizontal axis marine current turbines. Renewable energy, 32(15):2479–2490.
11. Nachtane, M., Tarfaoui, M., Goda, I., and Rouway, M. (2020). A review on the technologies, design considerations and numerical models of tidal current turbines. Renewable Energy, 157:1274–1288.
12. Ng, K.-W., Lam, W.-H., and Ng, K.-C. (2013). 2002–2012: 10 years of research progress in horizontal-axis marine current turbines. Energies, 6(3):1497–1526.

13. Vogel, C., Willden, R., and Houlsby, G. (2018). Blade element momentum theory for a tidal turbine. Ocean Engineering, 169:215–226.
14. Wekesa, D. W., Wang, C., Wei, Y., and Zhu, W. (2016). Experimental and numerical study of turbulence effect on aerodynamic performance of a small-scale vertical axis wind turbine. Journal of Wind Engineering and Industrial Aerodynamics, 157:1–14.
15. Bottasso, C. L., Campagnolo, F., and Petrovic´, V. (2014). Wind tunnel testing of scaled wind turbine models: Beyond aerodynamics. Journal of wind engineering and industrial aerodynamics, 127:11–28.
16. Devinant, P., Laverne, T., and Hureau, J. (2002). Experimental study of wind-turbine airfoil aerody-namics in high turbulence. Journal of Wind Engineering and Industrial Aerodynamics, 90(6):689–707.
17. Bayati, I., Belloli, M., Bernini, L., and Zasso, A. (2017). Aerodynamic design methodology for wind tunnel tests of wind turbine rotors. Journal of Wind Engineering and Industrial Aerodynamics, 167:217–227.
18. Hansen, M. (2015). Aerodynamics of wind turbines. Routledge.
19. Wilson, R. E. and Lissaman, P. B. (2018). Applied aerodynamics of wind power machines. Renewable Energy, pages Vol3 71–Vol3 120.
20. Burton, T., Jenkins, N., Sharpe, D., and Bossanyi, E. (2011). Wind energy handbook. John Wiley & Sons.
21. Manwell, J. F., McGowan, J. G., and Rogers, A. L. (2010). Wind energy explained: theory, design and application. John Wiley & Sons.
22. Letcher, T. (2023). Wind energy engineering: a handbook for onshore and offshore wind turbines. Elsevier.
23. Molland, A. F., Turnock, S. R., and Hudson, D. A. (2017). Ship resistance and propulsion. Cambridge university press.
24. Paraschivoiu, I. (2002). Wind turbine design: with emphasis on Darrieus concept. Presses inter Polytechnique.
25. Pacheco, A. and Ferreira, O´. (2016). Hydrodynamic changes imposed by tidal energy converters on extracting energy on a real case scenario. Applied Energy, 180:369–385.
26. Atcheson, M., MacKinnon, P., and Elsaesser, B. (2015). A large-scale model experimental study of a tidal turbine in uniform steady flow. Ocean Engineering, 110:51–61.
27. Malki, R., Williams, A., Croft, T., Togneri, M., and Masters, I. (2013). A coupled blade element momentum–computational fluid dynamics model for evaluating tidal stream turbine performance. Applied Mathematical Modelling, 37(5):3006–3020.
28. Mannion, B., Leen, S. B., and Nash, S. (2020). Development and assessment of a blade element momentum theory model for high solidity vertical axis tidal turbines. Ocean engineering, 197:106918.
29. Faudot, C. and Dahlhaug, O. G. (2012). Prediction of wave loads on tidal turbine blades. Energy Procedia, 20:116–133.
30. Zhu, F.-w., Ding, L., Huang, B., Bao, M., and Liu, J.-T. (2020). Blade design and optimization of a horizontal axis tidal turbine. Ocean Engineering, 195:106652.
31. Wang, L., Liu, X., Renevier, N., Stables, M., and Hall, G. M. (2014). Nonlinear aeroelastic modelling for wind turbine blades based on blade element momentum theory and geometrically exact beam theory. Energy, 76:487–501.
32. Sun, Z., Chen, J., Shen, W. Z., and Zhu, W. J. (2016). Improved blade element momentum theory for wind turbine aerodynamic computations. Renewable energy, 96:824–831.
33. Batten, W. M., Harrison, M., and Bahaj, A. (2013). Accuracy of the actuator disc-rans approach for predicting the performance and wake of tidal turbines. Philosophical Transactions of the Royal Society A: Mathematical, Physical and Engineering Sciences, 371(1985):20120293.
34. Guillou, S. S., Thie´bot, J., Santa Cruz, A., et al. (2016). Modelling turbulence with an actuator disk representing a tidal turbine. Renewable Energy, 97:625–635.
35. Du, L., Ingram, G., and Dominy, R. G. (2019). A review of h-darrieus wind turbine aerodynamic research. Proceedings of the Institution of Mechanical Engineers, Part C: Journal of Mechanical Engineering Science, 233(23-24):7590–7616.
36. Sadeqi, S., Xiros, N., Aktosun, E., VanZwieten, J., Sultan, C., Ioup, J., and Rouhi, S. (2021b). Power estimation of an experimental ocean current turbine based on the conformal mapping and blade element momentum theory. In ASME international mechanical engineering congress and exposition, volume 85628, page V07BT07A004. American Society of Mechanical Engineers.
37. Rouhi, S., Xiros, N., Aktosun, E., Sultan, C., VanZwieten, J., Ioup, J., and Sadeqi, S. (2021). A small-scale experimental ocean current turbine apparatus for power measurement. In ASME international mechanical engineering congress and exposition, volume 85628, page V07BT07A005. American Society of Mechanical Engineers.
38. Rouhi, S., Sadeqi, S., Xiros, N., Birk, L., Aktosun, E., and Ioup, J. (2022). Applying artificial intelligence to optimize small-

scale ocean current turbine performance. In ASME International Mechanical Engineering Congress and Exposition, volume 86670, page V005T07A067. American Society of Mechanical Engineers.

39. Sadeqi, S., Rouhi, S., Xiros, N., Aktosun, E., VanZwieten, J., Sultan, C., and Ioup, J. (2021a). Numerical investigation of an experimental ocean current turbine based on blade element momentum theory (bem). In International Conference on Offshore Mechanics and Arctic Engineering, volume 85192, page V009T09A002. American Society of Mechanical Engineers.
40. Flickinger, K. N. (2013). Facility development for testing small scale horizontal axis wind turbines.
41. Burdett, T. A. (2012). Aerodynamic design considerations for small-scale, fixed-pitch, horizontal-axis wind turbines operating in class 2 winds. PhD thesis.
42. 42.Musial, W. and McNiff, B. (2000). Wind turbine testing in the nrel dynamometer test bed. Technical report, National Renewable Energy Lab. (NREL), Golden, CO (United States).
43. Mohanty, B., Wang, F., and Stelson, K. A. (2019). Design of a power regenerative hydrostatic wind turbine test platform. JFPS International Journal of Fluid Power System, 11(3):130–135.
44. Mohanty, B. and Stelson, K. A. (2022). Dynamics and control of an energy-efficient, power- regenerative, hydrostatic wind turbine dynamometer. Energies, 15(8):2868.
45. Corbus, D., Baring-Gould, I., Drouilhet, S., Gevorgian, V., Jimenez, T., Newcomb, C., and Flowers, L. (1999). Small wind turbine testing and applications development. Technical report, National Renewable Energy Lab. (NREL), Golden, CO (United States).
46. Bahaj, A., Molland, A., Chaplin, J., and Batten, W. (2007b). Power and thrust measurements of marine current turbines under various hydrodynamic flow conditions in a cavitation tunnel and a towing tank. Renewable energy, 32(3):407–426.
47. Duhaney, J., Khoshgoftaar, T. M., Sloan, J. C., Alhalabi, B., and Beaujean, P. P. (2011). A dynamome-ter for an ocean turbine prototype: Reliability through automated monitoring. In 2011 IEEE 13th International Symposium on High-Assurance Systems Engineering, pages 244–251. IEEE.
48. Eriksson, S., Bernhoff, H., and Leijon, M. (2008). Evaluation of different turbine concepts for wind power. renewable and sustainable energy reviews, 12(5):1419–1434.
49. Hsiao, F.-B., Bai, C.-J., and Chong, W.-T. (2013). The performance test of three different horizontal axis wind turbine (hawt) blade shapes using experimental and numerical methods. Energies, 6(6):2784– 2803.
50. Viterna, L. A. and Janetzke, D. C. (1982). Theoretical and experimental power from large horizontal-axis wind turbines. Technical report, NASA Lewis Research Center, Cleveland, OH (United States).
51. Bai, C.-J. and Wang, W.-C. (2016). RevieM. Lewisw of computational and experimental approaches to analysis of aerodynamic performance in horizontal-axis wind turbines (hawts). Renewable and Sustainable Energy Reviews, 63:506–519.
52. Kishinami, K., Taniguchi, H., Suzuki, J., Ibano, H., Kazunou, T., and Turuhami, M. (2005). Theo- retical and experimental study on the aerodynamic characteristics of a horizontal axis wind turbine. Energy, 30(11-12):2089–2100.
53. Pope, K., Dincer, I., and Naterer, G. (2010). Energy and exergy efficiency comparison of horizontal and vertical axis wind turbines. Renewable energy, 35(9):2102–2113.
54. Lee, M.-H., Shiah, Y.-C., and Bai, C.-J. (2016). Experiments and numerical simulations of the rotor-blade performance for a small-scale horizontal axis wind turbine. Journal of Wind Engineering and Industrial Aerodynamics, 149:17–29.
55. Rouhi, S., Xiros, N. I., Sadeqi, S., and Birk, L. (2023). Dynamometer testing of hydrokinetic turbines in a towing tank facility. In ASME International Mechanical Engineering Congress and Exposition, volume 87639, page V006T07A097. American Society of Mechanical Engineers.
56. Hasankhani, A., VanZwieten, J., Tang, Y., Dunlap, B., De Luera, A., Sultan, C., and Xiros, N. (2021). Modeling and numerical simulation of a buoyancy-controlled ocean current turbine. International Marine Energy Journal, 4(2).
57. Jackson, R. S. and Amano, R. (2017). Experimental study and simulation of a small-scale horizontal-axis wind turbine. Journal of Energy Resources Technology, 139(5):051207.
58. Encarnacion, J. I., Johnstone, C., and Ordonez-Sanchez, S. (2019). Design of a horizontal axis tidal turbine for less energetic current velocity profiles. Journal of Marine Science and Engineering, 7(7):197.
59. Lotfy, K., Mahdy, A., El-Bary, A. A., and Elidy, E. (2024). Magneto-photo-thermoelastic excitation rotating semiconductor medium based on moisture diffusivity. CMES-Computer Modeling in Engineering & Sciences, 141(1).
60. Rouhi, S., Sadeqi, S., Xiros, N. I., Aktosun, E., Birk, L., and Ioup, J. (2024). Development of mathematical model for

coupled dynamics of small-scale ocean current turbine and generator to optimize hydrokinetic energy harvesting applications. Applied Sciences, 14(16).